

Coarse-Grained Model of SNARE Mediated Docking

Nicole Fortoul,[†] Pankaj Singh,[‡] Chung-Yuen Hui,[‡] Maria Bykhovskaia,[§] Anand Jagota,^{†¶}

[†]Department of Chemical and Biomolecular Engineering and [¶]Bioengineering Program, Lehigh University, Bethlehem PA 18017

[‡]Department of Mechanical & Aerospace Engineering, Cornell University, Ithaca, NY 14853

[§]Neuroscience Department, Universidad Central del Caribe, Bayamon, Puerto Rico

SUPPORTING MATERIAL

1. Coarse grain simulations: solution procedure

CG simulations were conducted for the 4 individual helices using Langevin dynamics at 300 K for a range of values of k_s . The Langevin equation (1) includes an inertial term, a viscous term, a random force term, and a potential energy term, respectively, in the form

$$m\ddot{x}(t) = -\gamma\dot{x}(t) + R(t) - \nabla E \quad (S1)$$

where m is the mass of each bead, $\ddot{x}(t)$ is the bead's acceleration at time t , γ is the damping constant, $\dot{x}(t)$ is the bead's velocity at t , $R(t)$ is a random force that represents the protein's interaction with the surrounding fluid, and E is the potential energy governing the solute that includes ENM forces. The fluctuation-dissipation theorem (2) connects the random force and viscous drag

$$\langle R(t) \cdot R(t') \rangle = 6\gamma k_B T \delta(t - t') \quad (S2)$$

where k_B is Boltzman's constant, T is temperature, $R(t')$ is the random force applied at t' , and $\delta(t - t')$ is the Dirac delta function. Written as a system of equations for all beads, the Langevin equation takes the form

$$[M]\{\ddot{u}(t)\} = -\gamma\{\dot{u}(t)\} + \{R(t)\} - [k]\{u(t)\} \quad (S3)$$

where $[M]$ is a diagonal mass matrix, $\{\ddot{u}(t)\}$, $\{\dot{u}(t)\}$, and $\{u(t)\}$ are column vectors containing the accelerations, velocities, and positions in the x, y, and z directions for each bead, $\{R(t)\}$ is a column vector containing the random force in the x, y, and z directions for each bead, and $[k]$ is a stiffness matrix.

The standard deviation of the random force is derived from Eqs. S2 and S3 to be

$$SD = \sqrt{\frac{2m\gamma k_B T}{\Delta t}} \quad (S4)$$

where Δt is the timestep. The friction coefficient is dependent on the bead type as well

$$\gamma = \frac{6\pi\eta a}{m} \quad (\text{S5})$$

where a is the Van der Waals radius of the bead and η is the viscosity of water. The timestep used for Langevin dynamics was based on the characteristic time, τ , that is defined as

$$\tau = \sqrt{\frac{m}{k_s}} \quad (\text{S6})$$

where m is the maximum bead mass. The timestep was adjusted to match the diffusion of a bead attached to a spring. Using this technique, the timestep was determined to be 43.4 fs or $\tau/20$.

In order to model the dynamics of the coarse-grained model, the Langevin dynamics equation was solved using a generalized Verlet algorithm (1)

$$\dot{x}^{n+1/2} = \dot{x}^n + m^{-1} \frac{\Delta t}{2} \left[-\nabla E(x^n) - \gamma M \dot{x}^n + R^n \right] \quad (\text{S7})$$

$$x^{n+1} = x^n + \Delta t \dot{x}^{n+1/2} \quad (\text{S8})$$

$$\dot{x}^{n+1} = \dot{x}^{n+1/2} + m^{-1} \frac{\Delta t}{2} \left[-\nabla E(x^{n+1}) - \gamma M \dot{x}^{n+1} + R^{n+1} \right] \quad (\text{S9})$$

where n is the timestep. The position is calculated from the half velocity, and then the position and half velocity are both used to calculate the full velocity.

2. ENM Reference State

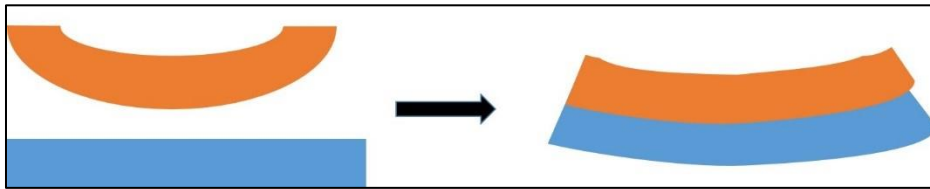


FIGURE S1 A model showing two beams. The reference or zero energy state for both beams is when they are separated from each other. When the beams form a bundle, mutual interactions deform them into some shape with associated stored energy that will be released when the beams are separated.

For each of the helices there exists a relaxed, natural, or reference state, and we maintain that the relaxed state of the springs that comprise the elastic network model should be defined in this reference state. This idea is illustrated in the figure above. Say we have two helices (orange and blue) with two different reference states (bent and straight). When the two helices come into contact with each other, they will both deform to form an equilibrium structure. If we assume the energy of the system to be 0 on the left, some energy is required to bend both helices to form the combined structure on the right. In our model we use our references states, like those on the left,

to help us calculate the energy stored in the bundle that can be released as the bundle is pulled apart.

The existence of such a reference state is not contingent upon its viability as a stable state for an actual isolated helix. Although Syb by itself is largely unstructured, we can still define the Syb helix by itself, i.e., removed from the other SNARE helices. It is a notional state used merely to obtain the frozen or stored elastic energy in the SNARE bundle. That is, all that is required is that the helical forms be stable as a bundle and that we have a systematic procedure by which to define springs on a relaxed state, again, regardless of whether the relaxed state actually exists.

We recognize that in many sources in the literature it is noted that Syb is largely unstructured when not in the presence of the SNARE bundle. We conducted 40 ns all-atom simulation of the individual SNARE helices, starting with a configuration extracted from the crystal structure. We found that this timescale was more than sufficient to allow all of the helices to straighten into relatively straight rod-like conformations. It was also short enough that each rod retained its helical structure. Because of this separation of time scales – time to relax an individual helix \ll time required for it to lose its structure – we were able to define the natural or reference state of each helix on which to construct the elastic spring network.

3. Determining the cut-off distance and spring constant in the elastic network model for SNARES

Coordinates from the straightened out helical structures were extracted from the individual AA simulations, and the connectivity and natural length of the ENM springs for each helix were determined based on these structures. If the cutoff distance is too small, the proteins will denature. If it is too large, simulation speed will be compromised with no significant improvement in representation. In order to find an optimal value, this distance was adjusted and a histogram was created for each helix to show the total number of springs that were connected to each bead. The minimum criterion for the number of springs was that each bead should be connected by a spring to all of its nearest neighbors. It was concluded that a cutoff distance of a minimum of 10 Å yielded at least 4 springs per bead, which satisfied this criteria. After further investigation, it was determined that R_c was required to be at least 20 Å in order to maintain the helical structure of each helix during AA simulations. The histogram for the final value of R_c , 20 Å, for the helix Syb is shown in Fig. S2. The histograms for the other three helices are similar.

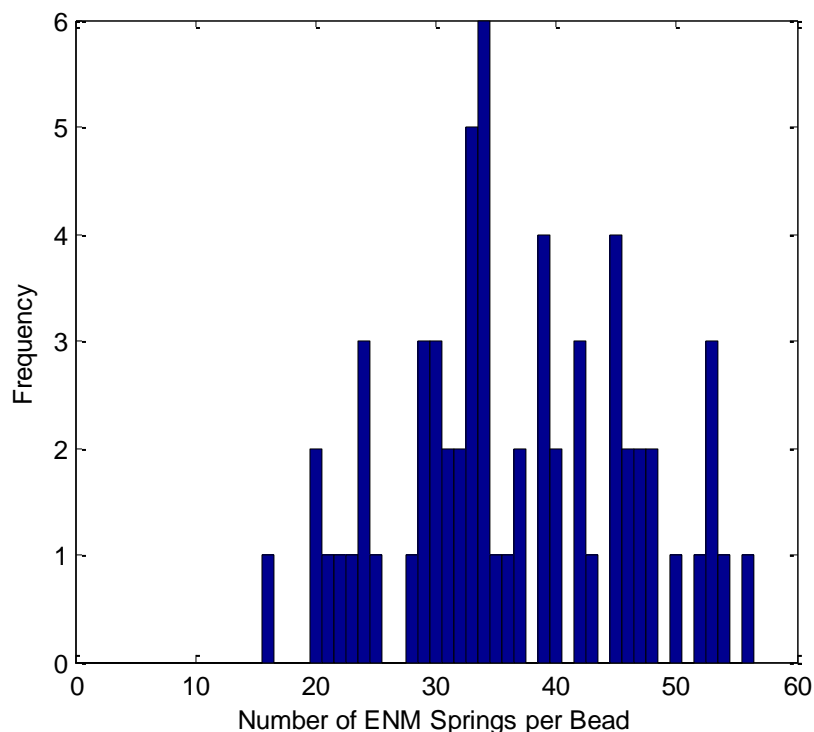


FIGURE S2 A histogram for the number of ENM springs per bead is shown for Syb with a value of 20 \AA for R_c .

The values of k_s for the ENM were chosen by matching the spectrum of fluctuations of the AA simulations and the CG model. For the analysis of individual AA helix simulations, the positions of the alpha carbons were extracted every 10 ps. For each alpha carbon a time series of distance from average location was calculated. The fast Fourier transform (FFT) was then evaluated for each bead's time series. The average was taken over all beads yielding a single spectrum per helix. In order to make this comparison of the fluctuations, CG simulations were conducted for the 4 individual helices using Langevin dynamics at 300 K for a range of values of k_s . The time length of simulations required was determined by conducting a normal modes analysis (NMA) on the CG model of the crystal structure, 1N7S, for all helices individually using different values of k_s . AA simulations were run for 2 ns, which is considerably longer than the characteristic time given as the inverse of the lowest natural frequency. The results for Syb are shown in Table S1.

TABLE S1 The lowest natural frequencies and characteristic times for Syb determined are shown below for different values of k_s

k_s (N/m)	Lowest Natural Frequency Squared (1/ns) ²	Time (ns)
0.0963	4.53	4.70E-01
0.1926	9.05	3.32E-01
0.2889	1.36	2.71E-01
0.3853	1.81	2.35E-01
0.4816	2.26	2.10E-01

For Syb, as was seen for all helices, the characteristic times are significantly less than 1 ns. As a result the AA simulations were analyzed for the first 2 ns of the trajectories, and the CG test simulations were conducted for 2 ns and analyzed with data collected every 2 ps. In order to best match the fluctuations, the root mean squared deviation (RMSD) between the AA and CG spectra was found for each run. An example of the comparison of both spectra is shown in Fig. S3 for Syb with k_s value of 0.0963 N/m. The RMSD for all helices for all values of k_s are shown in Table S2 with the minimum RMSD values shaded in grey.

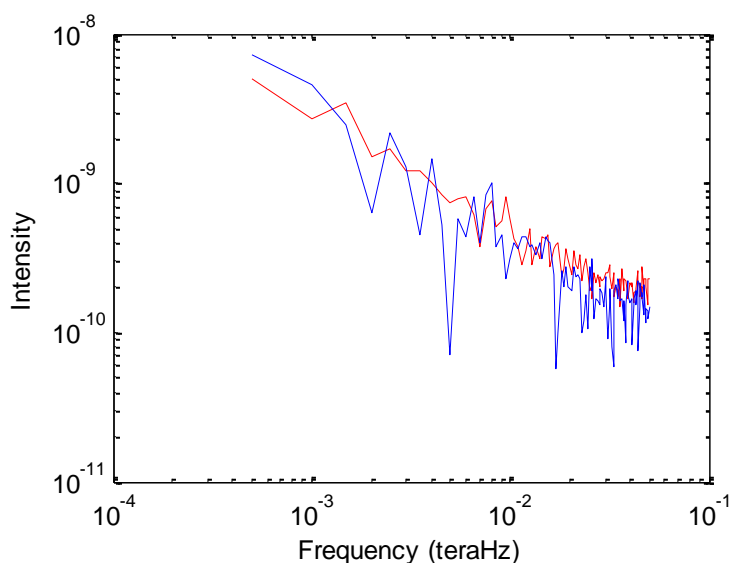


FIGURE S3 The spectra used to compare the fluctuations of the AA (*blue*) and CG (*red*) models are shown for Syb for 2 ns. Values of k_s as 0.0963 N/m and R_c of 20 Å were used for the CG model. An RMSD of 4.7E-10 was found.

TABLE S2 The RMSD values between the AA and CG fluctuation spectra are shown below for all helices for a range of values of k_s . The minimum RMSD values are shaded in grey.

k_s (N/m)	Syb RMSD	Syx RMSD	SN1 RMSD	SN2 RMSD
0.00009	9.6450e-09	1.0532e-08	1.2658e-08	9.5905e-09
0.0009	4.9432e-09	5.5075e-09	6.7327e-09	4.6640e-09
0.0096	1.4341e-09	1.1056e-09	1.5941e-09	1.7538e-09
0.0481	7.4334e-10	1.4651e-09	8.5729e-10	1.6778e-09
0.0963	4.7077e-10	4.3346e-10	1.3671e-09	2.3080e-09
0.1444	7.2271e-10	9.9229e-10	1.5680e-09	1.1604e-09
0.1926	1.4341e-09	1.1064e-09	1.5941e-09	1.7539e-09
0.2889	1.2019e-09	1.5654e-09	2.7382e-09	3.0644e-09
0.3853	1.7372e-09	2.0310e-09	3.2207e-09	3.3413e-09
0.4816	2.4969e-09	2.8429e-09	3.2951e-09	3.5652e-09

Based on the data in Table S2, a value of 0.0963 N/m was chosen for k_s for all four helices. For Syb and Syx, this corresponds to the value of k_s with the smallest RMSD. For SN1 and SN2 however, the minimum RMSD occurs either a little above or below k_s of 0.0963 N/m. Because the RMSD is still very small for these two helices with that value of k_s , it was chosen to use a consistent value of k_s for all helices.

4. Calibration of λ and displacement orientation

As described in the SNARE CG model portion in the methods section, the value of λ was adjusted in order to match the peak force reported by Gao et al. (3) of 14 – 19 pN. We conducted a series of displacement control simulations at 0K for a set of λ values ranging from 0.30 to 0.72. Displacement was applied in steps and the system allowed to relax. Relaxation to equilibrium was monitored by tracking the forces acting on the C-terminal beads of Syb and Syx as shown in Fig. S4. Each force spike corresponds to a displacement being applied to the C-terminal bead of Syb. After 10^5 timesteps, both forces relax to nearly the same value, which is taken as the equilibrium force for that displacement, and the next displacement step is then applied.

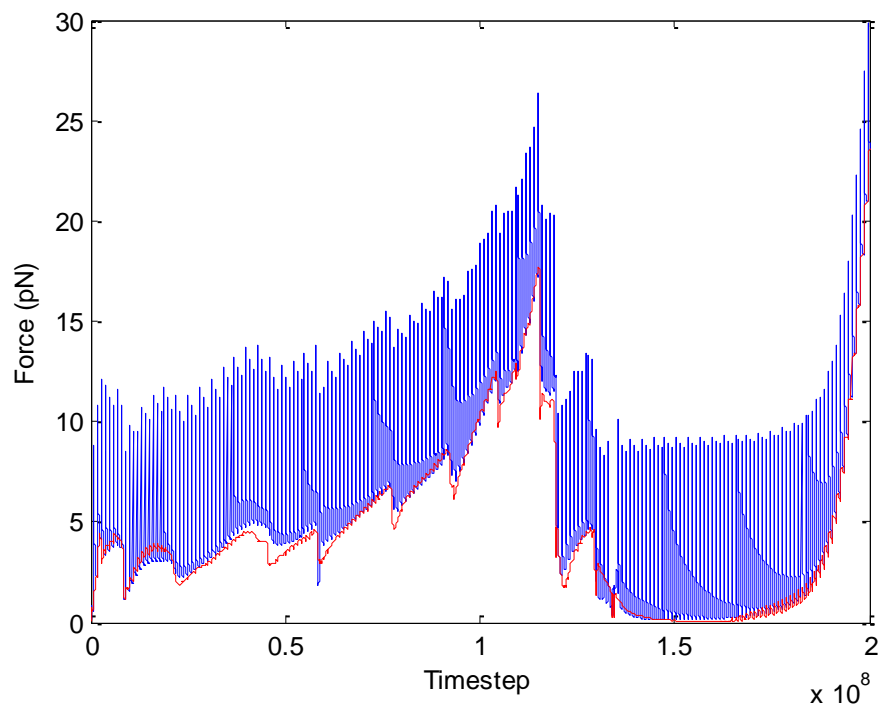


FIGURE S4 The force as a function of timestep is shown for a displacement control run with λ set to 0.30. The forces on the C-terminal beads of Syb (*blue*) and Syx (*red*) are shown. Each spike in the Syb force corresponds to application of a new displacement step. A total displacement of 20 nm is shown.

The resulting force displacement curves for a few of these runs for varying λ are shown in Fig. S5.

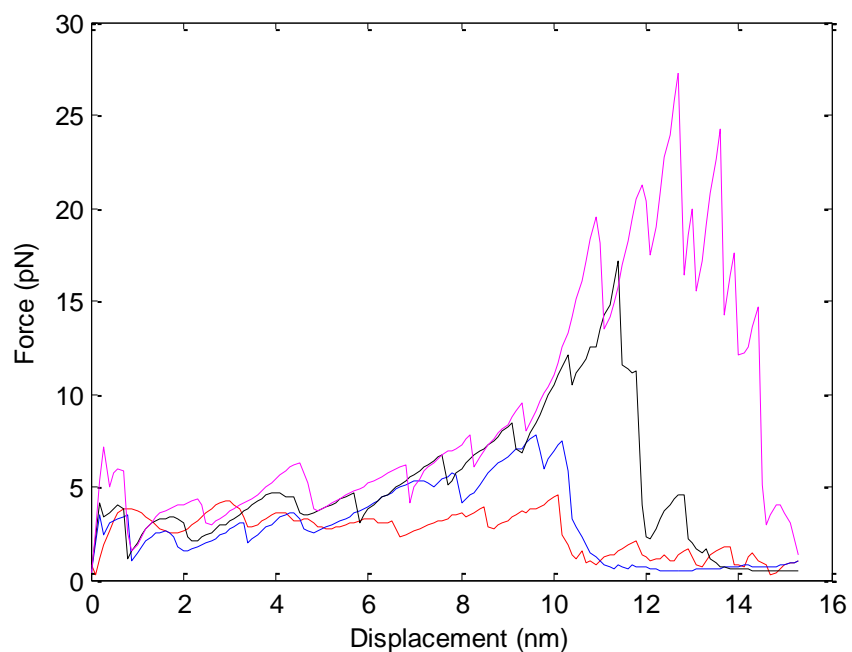


FIGURE S5 Force displacement curves are shown for displacement control simulations done using λ values of 0.16 (*red*), 0.24 (*blue*), 0.30 (*black*), and 0.40 (*magenta*).

It was clear that as λ was increased, the peak force increased as well. By choosing its value to be 0.3, we attained a peak force of 17.2 pN that lies in the experimentally measured range.

5. SNARE Force Displacement Instabilities and Their Effect on Energy

There are several mechanical instabilities in the force-separation curve of the SNARE, for example at 7.5 nm in Fig. 3 C. These usually correspond to “breaking” of one of the layers. When the system jumps from one stable point to the next, it does not follow the equilibrium force-separation relationship between these two points; instead, it lies above it. When we integrate the force-separation curve to obtain energies, we consequently compute a slightly larger magnitude (more negative) than it should be. This does not affect any of the predictions about stable equilibria.

6. Continuum Governing Equations and Their Solution

The axisymmetric deformation of the vesicle-membrane system can be reduced to the solution of a set of ordinary differential equations. The undeformed configuration of the vesicle is a sphere of radius R with arc-length in a cross-section denoted by S whereas, the plasma membrane occupies the interior of a circle of radius $L \ll R$. We introduce the notation ϕ to denote the angle made by the tangent to a point on the cross-section of the deformed membrane in the (r, z) plane with the z axis (see Fig. S5 A). Briefly, the equations describing the deformation involve the shear force Q , the angle ϕ , the mean curvature H , the deformed arc length ξ , the deformed coordinates of a generic material point (r, z) which has an arc length coordinate S in the undeformed configuration. To expedite the analysis, we introduce the following normalized variables:

$$\begin{aligned} \bar{S} &= \frac{S}{R}, \quad \bar{r} = \frac{r}{R}, \quad \bar{z} = \frac{z}{R}, \quad \bar{H} = RH, \quad \bar{\xi} = \frac{\xi}{R}, \\ \bar{Q} &= \frac{QR^2}{c}, \quad \bar{d} = \frac{dR^2}{c}, \\ \bar{p}_0 &= \frac{p_0 R^3}{c}, \quad \bar{F}_e = \frac{F_e R^3}{c}, \quad \bar{F}_n = \frac{F_n R^3}{c}, \quad \bar{F}_t = \frac{F_t R^3}{c}, \end{aligned} \tag{S10}$$

where,

p_0 is the osmotic pressure of the vesicle,

d is an integration constant resulting from integrating the tangential force equilibrium equation (see supplementary information for details),

F_e is the electrostatic force per unit area of the membrane and is always along z direction,

F_t is the tangential component of the concentrated load at the material point S_0 in the deformed membrane,
 F_n is the normal component of the concentrated load at the material point S_0 deformed membrane.

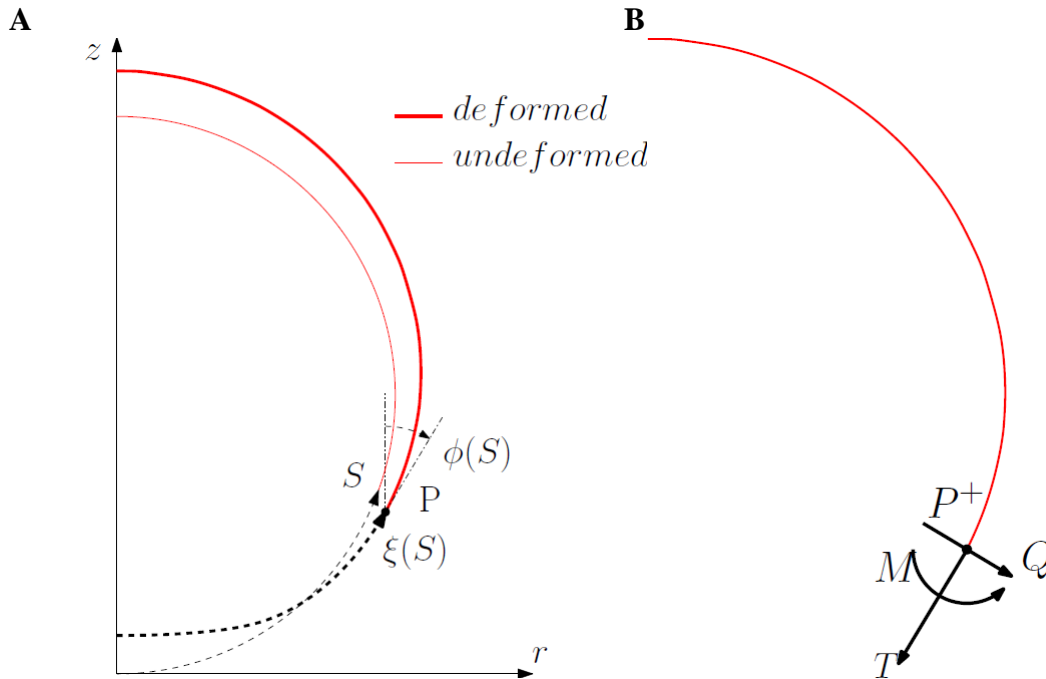


FIGURE S6 (A) Arc length and tangent angle over the membrane, (B) Forces and moment along the cut in the membrane.

As shown above non-dimensionalization of all the length scales is done by the radius of the undeformed vesicle, R . As c has units of energy, we use it to non-dimensionalize force per unit length quantities i.e. in-plane tension, T and out of plane shear, Q by c/R^2 . Also force per unit area quantities, p_0, F_e, F_t and F_n are made dimensionless by c/R^3 .

Also, in both the loading conditions it has been assumed that the F_t for vesicle is always zero. There are six ordinary differential equations governing the deformation of the vesicle membrane, they are:

$$\begin{aligned}
\dot{Q} &= -\frac{\bar{Q}}{\bar{r}} \dot{\xi} \sin \phi - 2\bar{H} \dot{\xi} \left[\bar{d} + \bar{H}^2 + \left(2\bar{H} + \frac{\cos \phi}{\bar{r}} \right) \frac{\cos \phi}{\bar{r}} \right] + \dot{\xi} \bar{P}, \\
\dot{\phi} &= \dot{\xi} \left(2\bar{H} + \frac{\cos \phi}{\bar{r}} \right), \\
\dot{H} &= \dot{\xi} \bar{Q}, \\
\dot{r} &= \dot{\xi} \sin \phi, \\
\dot{z} &= \dot{\xi} \cos \phi, \\
\dot{d} &= \left(\bar{F}_e \cos \phi + \bar{F}_t \right) \dot{\xi}
\end{aligned} \tag{S11a-S11f}$$

where, the dot denotes differentiation with respect to the normalized undeformed arc length \bar{S} , and

$$\dot{\xi} \equiv \frac{\sin \bar{S}}{\bar{r}}. \tag{S11g}$$

The normalized normal force acting on the deformed membrane surface, \bar{p} in Eq. S11a is related to the osmotic pressure of the vesicle, \bar{p}_0 , the electrostatic force per unit area, \bar{F}_e and the normal component of the concentrated load applied at $\bar{S} = \bar{S}_0$, \bar{F}_n by,

$$\bar{p} = \bar{p}_0 + \bar{F}_e \sin \phi + \bar{F}_n \delta(\bar{S} - \bar{S}_0) \tag{S11h}$$

where, $\delta(\bar{S} - \bar{S}_0)$ is the Dirac delta function.

These differential equations are supplemented with the boundary conditions:

$$\begin{aligned}
\phi(\bar{S} = 0) &= \frac{\pi}{2}, \\
\bar{Q}(\bar{S} = 0) &= 0, \\
\bar{r}(\bar{S} = 0) &= 0, \\
\phi(\bar{S} = \pi) &= -\frac{\pi}{2}, \\
\bar{Q}(\bar{S} = \pi) &= 0, \\
\bar{r}(\bar{S} = \pi) &= 0,
\end{aligned} \tag{S12a-S12f}$$

The boundary conditions defined above essentially represent the symmetry in the vesicle geometry. About the symmetry axis, the curve has zero slope and out of plane shear \bar{Q} is zero, at both $\bar{S} = 0$ and π . Also, for the continuity of the geometry, we impose $\bar{r} = 0$ at both $\bar{S} = 0$ and π .

The notation for positive shear force and tension is described in Fig. S6. Finally, the expression for the in-plane tension in both the vesicle and plasma membrane is given by,

$$\bar{T} = \frac{TR^2}{c} = \frac{R^2}{c} \left(-d - cH^2 - cH \frac{\cos\phi}{r} \right). \quad (S13)$$

The governing equations for the deformation of the plasma membrane is very similar, except that Eq. S11g must be replaced by,

$$\dot{\bar{\zeta}} = \frac{\bar{S}}{\bar{r}} \quad (S14)$$

This change is due to the difference between the reference configurations. The boundary conditions are:

$$\begin{aligned} \phi(\bar{S}=0) &= \frac{\pi}{2}, \\ \bar{Q}(\bar{S}=0) &= 0, \\ \bar{r}(\bar{S}=0) &= 0, \\ \phi\left(\bar{S} = \frac{L}{R}\right) &= \frac{\pi}{2}, \\ \bar{z}\left(\bar{S} = \frac{L}{R}\right) &= 0, \\ \bar{T}\left(\bar{S} = \frac{L}{R}\right) &= \left[-\bar{d} - \bar{H}^2 - \bar{H} \frac{\cos\phi}{\bar{r}} \right]_{\bar{S}=\frac{L}{R}} = \bar{T}_0 = \frac{T_0 R^2}{c} \end{aligned} \quad (S15a-S15f)$$

The boundary conditions at $\bar{S} = 0$ is due to axisymmetry. Eq. S15f states that the tension in the plasma membrane approaches the pretension at the boundary. This boundary condition allows the neuron membrane to deflect. Had we replaced this boundary condition with a clamped condition, the deflection everywhere would be zero because of area incompressibility.

The coupled ODE's in Eqs. S11 - S15 with the boundary conditions are solved using the MATLAB® bvp4c solver. The input parameters for the solver are the osmotic pressure p_0 across the vesicle membrane which remains fixed throughout the deformation, SNARE-machinery force parameters (S_0 and magnitude F), electrostatic force and pretension (T_0) in the plasma membrane.

7. Example problem of continuum model

Here we show an example of the results of the calculation of vesicle-membrane interaction. In

this example, the location of force application is fixed at $\bar{S}_0 = \frac{\pi}{6}$ on both the vesicle and neuron

base, as shown in Fig. S7. This location of load application corresponds to the number of SNAREs of 21. Parameters used in the continuum model are shown in Table S3.

TABLE S3 Parameters used for the continuum model of the vesicle and plasma membrane

Parameter	Value	Comment
Permittivity of vacuum, ϵ_0	$8.85 \times 10^{-12} \text{ Fm}^{-1}$	

Dielectric constant of water, ϵ	80	dimensionless
Ion concentration inside neuron, c_0	200 mM (4)	(1-1) electrolyte
Debye length, l_D	0.67nm	$l_D = \sqrt{\frac{\epsilon\epsilon_0 k_B T}{2q^2 z^2 c_0}}$
Synaptic vesicle radius, R	20nm (5)	
Surface charge of vesicle and inside of plasma membrane, σ_1 and σ_2	-0.025 Cm^{-2} , -0.025 Cm^{-2} (5–7)	
Surface potential of vesicle and inside of plasma membrane, φ_1 and φ_2	-25 mV , -25 mV	
Bending rigidity of lipid bilayer, c	$\sim 20 \text{ k}_B T$ (8)	$8.28 \times 10^{-20} \text{ J}$

The strength of the line force is varied in the range of 5–20 in dimensionless terms, which is equivalent to a net force between 66–266 pN. Fig. S7 shows the deformed shapes of the membranes for four different values of \bar{F} . The inset on the right shows the calculated relationship between applied force and separation between load application points. The force decreases rapidly with increasing separation, reflecting the steep decay of the electrostatic repulsion.

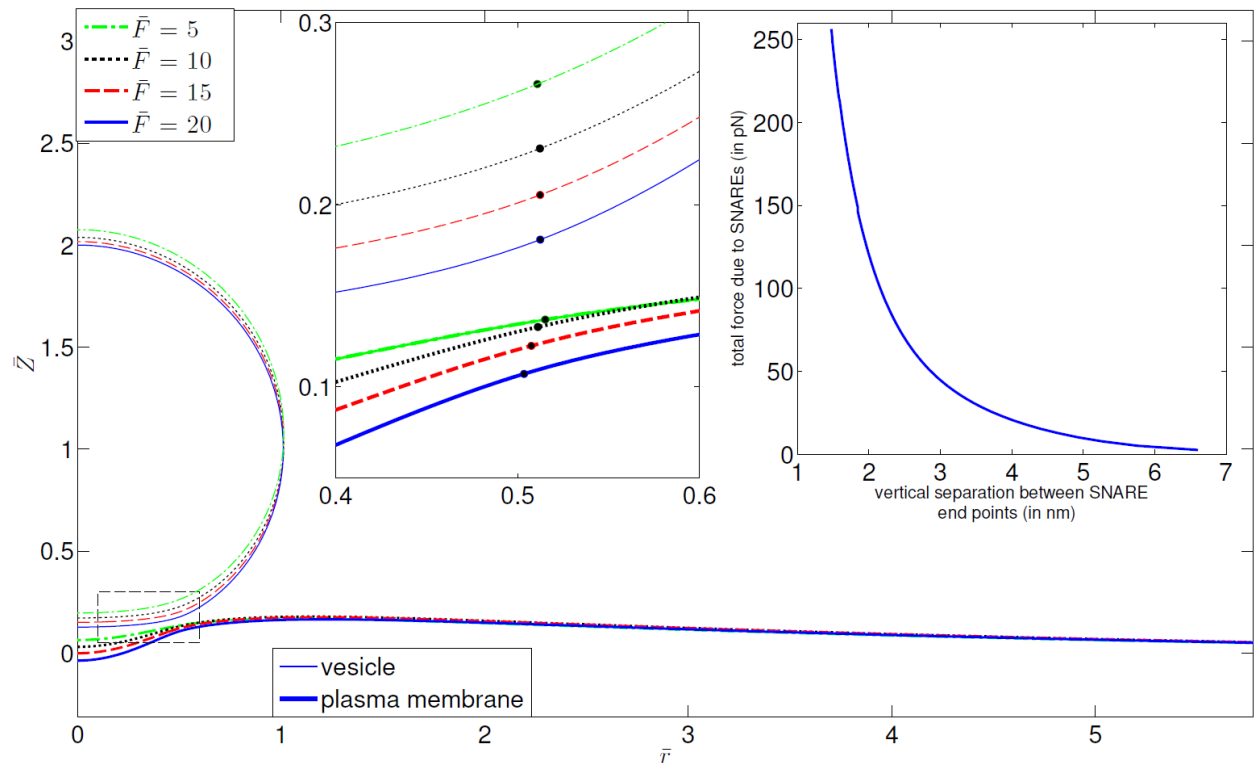


FIGURE S7 Deformed geometry for different force magnitudes. The thick lines represent the neuron base and the thin lines represent the vesicle. The inset on the left shows the zoomed in section of the load application point (shown as \bullet) and the inset on the right shows the vertical separation between the two ends of SNARE-machinery versus the net SNARE force. The

parameters are for the analysis are: load application point, $\bar{s}_0 = \pi/6$, pretension in plasma membrane, $\bar{t}_0 = 1$ and vesicle pressure. $\bar{p}_0 = 1$.

8. SNARE Force Separation Curve Shift

To compare the attractive force imposed by the SNARE bundle to the repulsive force on the vesicle, we need a consistent definition of separation. The distance connecting the final residue beads (Syb89 and Syx256) is shorter than the distance between the outside membrane surfaces due to the presence of other parts of the SNARE. To address this issue, we created a static coarse grained structure of a 20 nm vesicle and plasma membrane with a partially opened SNARE at its equilibrium configuration as shown in the figure below. We found that distance between the outer surface of the membranes is actually about ~ 1 nm further apart than the distance between Syb89 and Syx256. We have therefore added this distance when comparing the attractive force on the SNARE to the repulsive force on the vesicle. Adding the initial separation between Syb89 and Syx256, the minimum distance allowed between the membranes at the point of force application is about 2 nm. Another related effect is that inter-SNARE-bundle repulsion can increase the minimum lateral separation. We have considered two additional cases where we take lateral SNARE bundle width to be 2 and 4 nm (an additional Debye screening length increase in radius in the latter case). The larger lateral spacing makes the effect of number of SNAREs significantly stronger but the minimum separation and the number of SNAREs needed to achieve it does not change much.

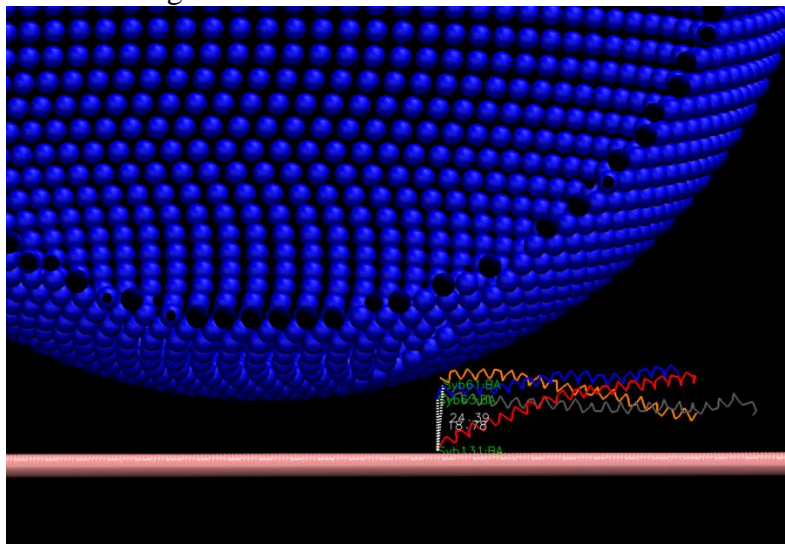


Figure S8. Drawing of a vesicle near a plane along with a model for the SNARE bundle.

9. Choice of SNARE Model

The CG simulation model was built using the SNARE X-ray crystal structure 1N7S that includes Syb (27-89), Syx (189-256), SN1 (5-83), and SN2 (139-204). We recognize that this structure only includes part of the Syb linker domain (85-95) and none of the linker domain of Syx (256-266). However, we believe that our choice of placing the membrane outer surface at residues 89 and 256 is correct. Our choice is based on the following papers (9, 10) that show Syb insertion in the membrane starts at Trp 89. Specifically, they show that 89-94 is unstructured but is

inserted in the membrane. Similarly, the following paper shows that for Syx, residues after 261 are in the lipid bilayer. Specifically, 261-266 are unstructured but inside the lipid bilayer (11). The following study (12) also concludes that the linker domains (256-266) and (85-95) are buried in the top layer of the membrane. Because the reference distance from the hydration repulsion is the outer surface of the membrane, to be consistent we believe that it is quite appropriate to define SNARE displacement from 88 for Syb to 256 for Syx, within some uncertainty of a just a few residues.

Whether or not the linker domains have unraveled is debatable. It was shown in Gao et al's optical tweezer experiment that the Syb linker domain unravels at 10-13 pN. Because the equilibrium SNARE end-end distances of interest in this work are $< \sim 3$ nm), our maximum force only reaches (< 5 pN) and neglecting helix unraveling in our model is justifiable. Nevertheless, in order to check the robustness of our solution against unraveling, we did melt two helical turns of Syb (including up to residue 91). The principal effect is that the minimum equilibrium separation increases from 2 nm to 2.5 nm for both hydration and electrostatic repulsion with a constant charge.

10. Robustness of Model Results

To judge the sensitivity of our main conclusions on the various assumptions we have made, we carried out a number of other simulations. Our main conclusion is that the principal results of our model are quite robust with respect to uncertainty in the assumptions made.

10.1. Electrostatics: We explored how electrostatics would affect the vesicle to plasma membrane repulsion. Fig. S9 shows results for the case where hydration repulsion is replaced by electrostatics using a fixed surface charge of -0.025 C/m^2 on the vesicle and the membrane. Evidently, with these parameters the electrostatic repulsion is weaker than the hydration repulsion. For one SNARE the end separation is ~ 2.4 nm, which is smaller than the 3 nm seen for the hydration repulsion case (Fig. 4 B). However, when more than 1 SNARE is added to the system, the equilibrium SNARE end separation is constant at ~ 2 nm for 2-13 SNAREs, that is, it would be completely zippered shut.

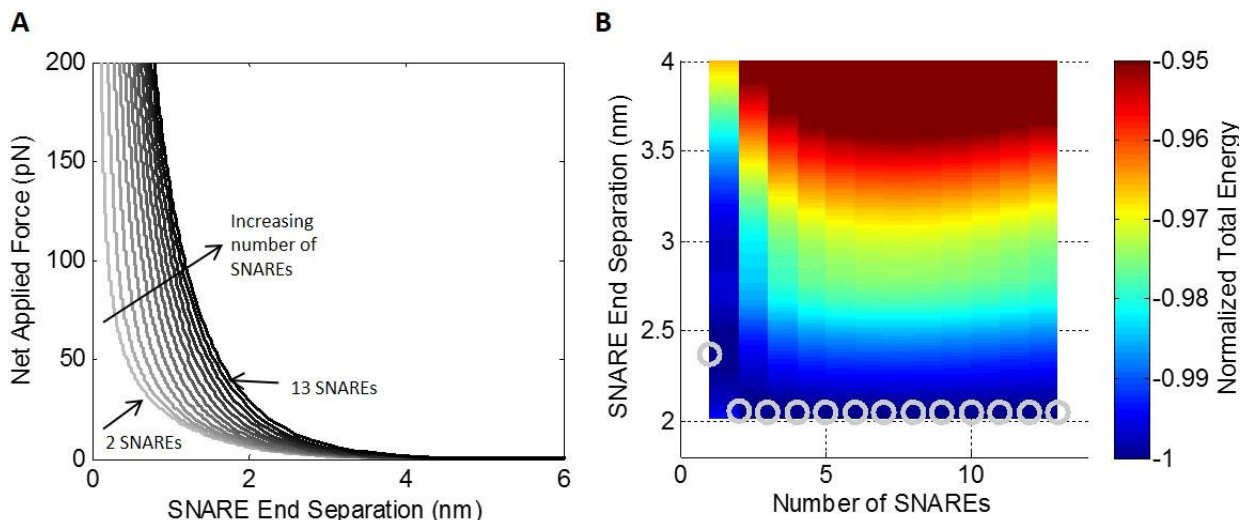


FIGURE S9 (A) The force in the membrane/vesicle system is shown as a function of SNARE end separation for a vesicle radius of 20nm with electrostatic repulsion with a fixed surface charge. (B) The corresponding contour plot of total energy as a function of SNARE end

separation distance and the number of SNAREs. Gray circles correspond to global energy minima representing the equilibrium SNARE end separation for a given number of SNAREs.

10.2. Larger vesicles: Although our primary interest is in the smaller synaptic vesicles, the model can also be applied to study larger vesicles. Fig. S10 shows results for the case of a 100 nm vesicle.

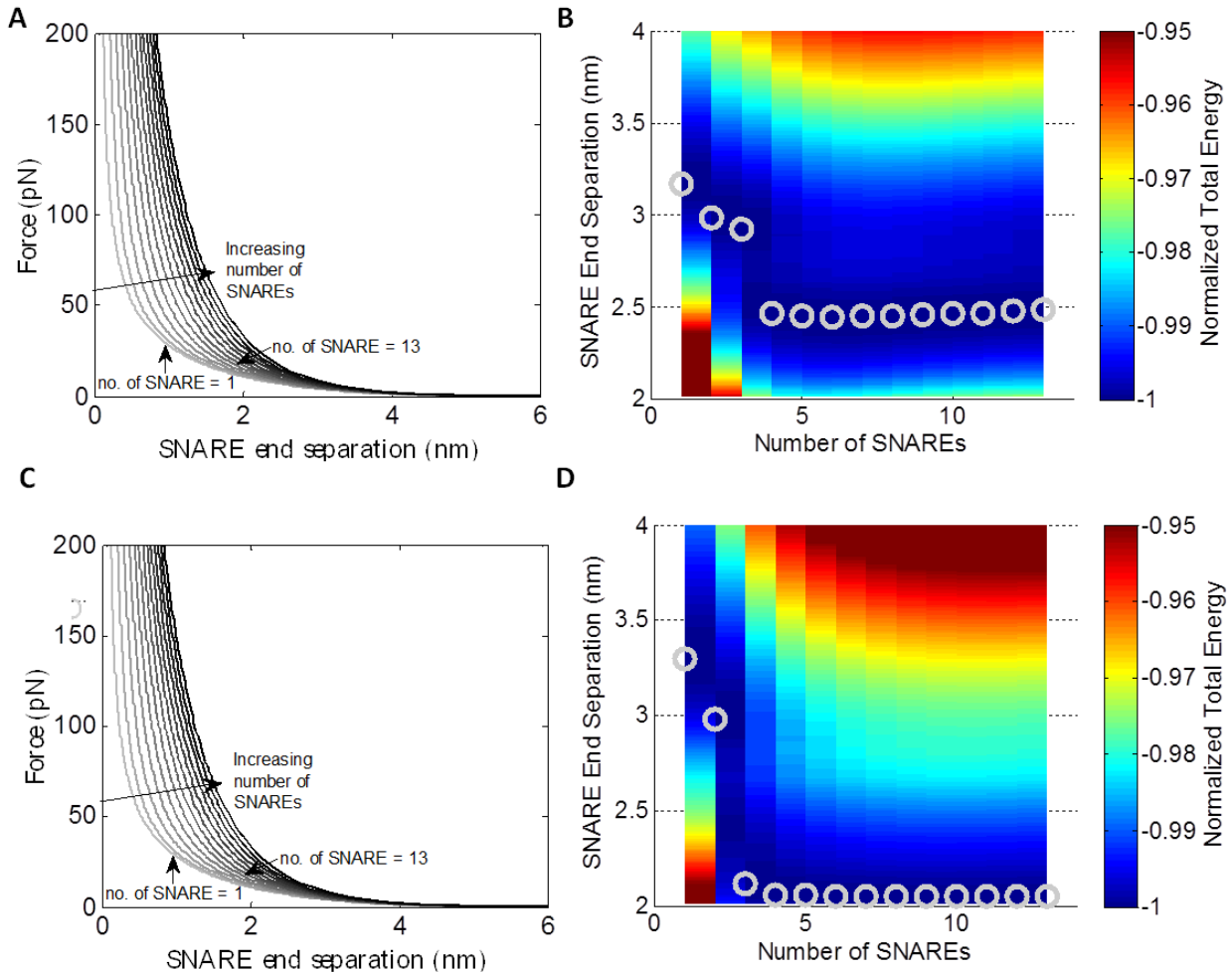


FIGURE S10 The force in the membrane/vesicle system is shown as a function of SNARE end separation for a vesicle radius of 100nm with (A) hydration repulsion and (C) electrostatic repulsion with a fixed surface charge. Contour plots of total energy as a function of SNARE end separation distance and the number of SNAREs are shown for a vesicle radius of 100nm with (B) hydration repulsion and (D) electrostatic repulsion with a fixed surface charge. Gray circles correspond to global energy minima representing the equilibrium SNARE end separation for a given number of SNAREs.

For the hydration repulsion case the minima are significantly larger than those found for the 20nm case shown in Fig. 4 B. For four or more SNAREs the equilibrium separation is ~ 2.5 nm which is different from the 20nm case where the separation is ~ 2 nm and the SNARE bundle can be nearly fully zippered. For the case of electrostatic repulsion, for larger number of SNAREs the repulsion is still insufficient to open the SNARE except when there is are three or fewer SNAREs.

10.3. Fixed Potential: We also carried out computations assuming a fixed potential of -25 mV on the vesicle and on the membrane as opposed to the fixed surface charge case that was assumed in the majority of the paper. The resulting force separation curves for the 20nm and 100nm vesicle cases are very similar to the case of fixed charge. This is not unexpected because the electrostatic force for fixed charge versus fixed potential cases becomes nearly the same for separations greater than the Debye screening length.

10.4. Unraveling of Syb: Several other modifications were made to the cases shown in Fig. 4. There is some question about whether part of the syb helix unravels. We have argued that the forces are small enough that the helical structure should be preserved. However, to test the effect on our prediction of potential unraveling, we allowed 2 helical turns to unravel and be represented by elasticity of a worm-like chain coil. Because the Syb helix touches the membrane at residue 91 and the CG model only contains up to residue 89, an extra 2 residues were added to the unraveled portion of Syb. The force displacement curve for the melted portions of Syb were modeled using a worm like chain model following Gao et al.(3) The force extension relationship was calculated using the Marko-Siggia formula

$$F = \frac{k_B T}{P_{melt}} \left[\frac{1}{4 \left(1 - \frac{x_{melt}}{L_{melt}} \right)^2} + \frac{x_{melt}}{L_{melt}} - \frac{1}{4} \right] \quad (S16)$$

where P_{melt} is the persistence length of the melted segment (0.6 nm) and x_{melt} is the end to end distance of the melted segment. L_{melt} , the maximum end to end distance of the melted segment, was calculated assuming a 0.365 nm contour length per residue (3) which totaled to 1.3 nm due to ~2 helical turns being melted. The master force displacement curve was slightly adjusted by deleting the portions of the curve that corresponded to the 7 residues that are now accounted for using the WLC model. The SNARE end separation, x_{SNARE} , was defined by

$$x_{SNARE}(F) = x_{melt}(F) + x_{bundle}(F) + BW \quad (S17)$$

where x_{melt} is the end to end distance of the melted portion of Syb, x_{bundle} is described using the manipulated master force curve described in this section, and BW is the width of the SNARE bundle or the distance between the Syb and Syx C-termini when no external force is being applied. The corresponding results are shown in Fig. S11 A for a 20nm vesicle with hydration repulsion and Fig. S12 A for a 20nm vesicle with electrostatic repulsion and a fixed surface charge.

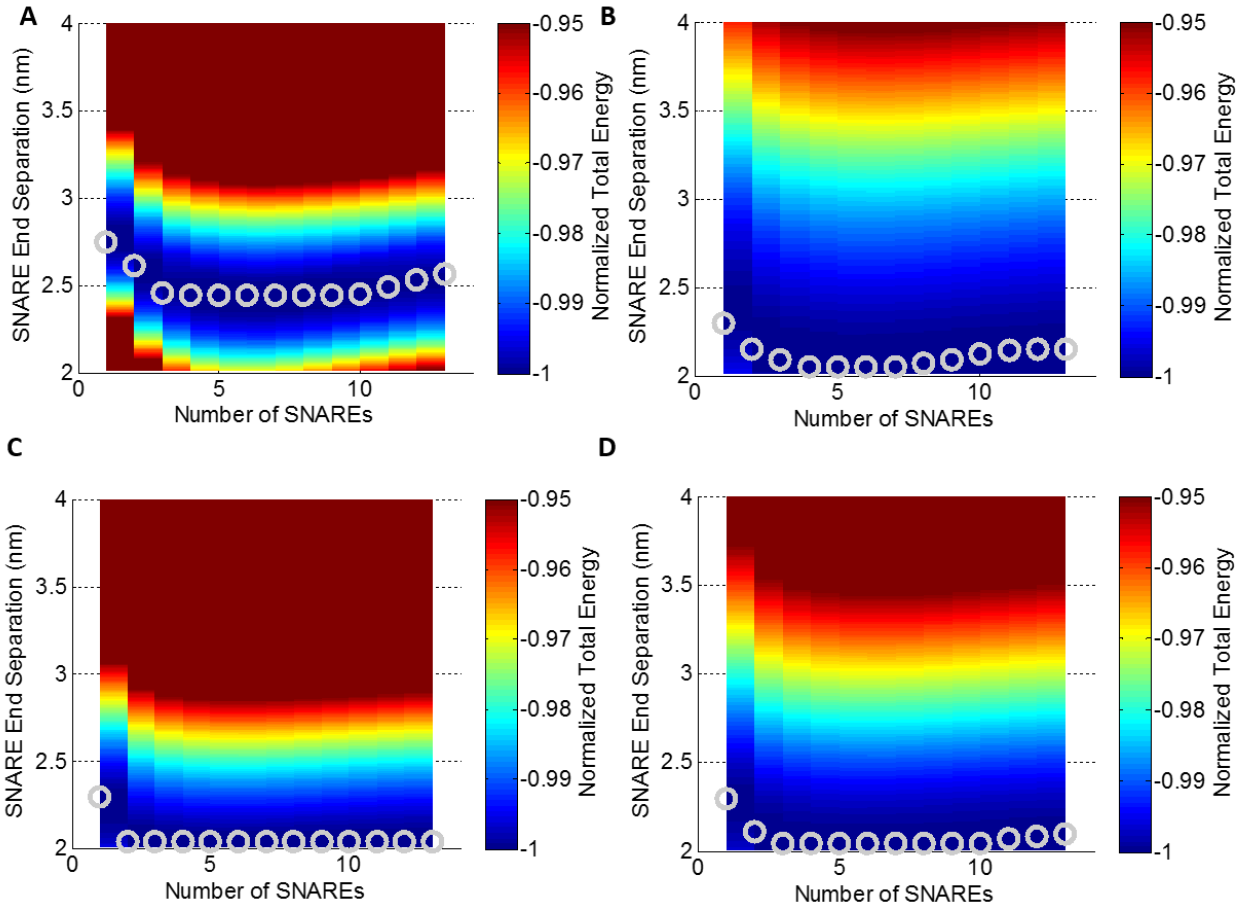


FIGURE S11 For a 20nm vesicle with hydration repulsion, contour plots of normalized total energy as a function of SNARE end separation distance and the number of SNAREs are shown. Gray circles correspond to energy minima representing the equilibrium SNARE end separation for a given number of SNAREs. Several cases are shown: (A) 2 helical turns unraveled, (B) Syx frozen, (C) SNAP25 frozen, and (D) Syx and SNAP25 frozen.

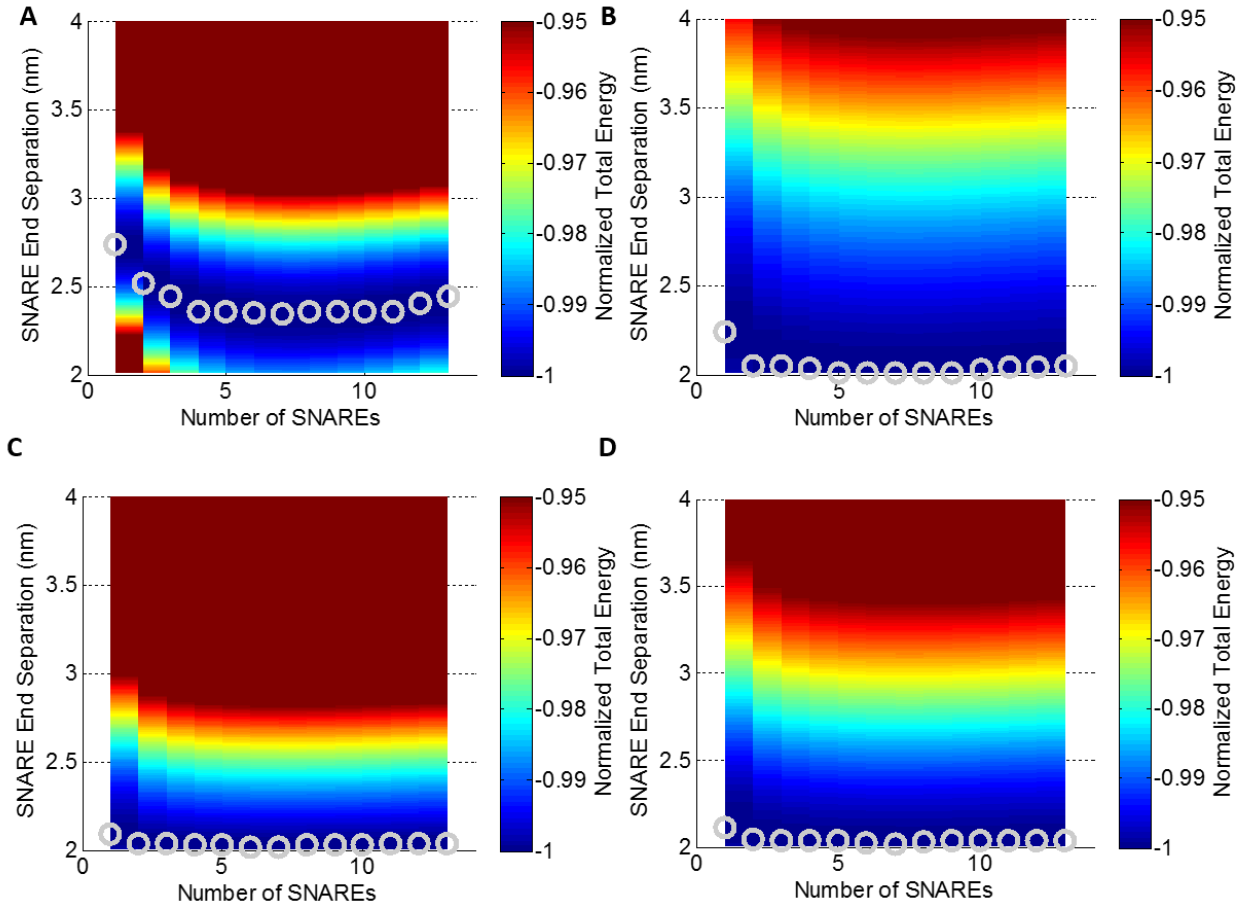


FIGURE S12 For a 20nm vesicle with electrostatic repulsion assuming a fixed surface charge, contour plots of normalized total energy as a function of SNARE end separation distance and the number of SNAREs are shown. Gray circles correspond to energy minima representing the equilibrium SNARE end separation for a given number of SNAREs. Several cases are shown: (A) 2 helical turns unraveled, (B) Syx frozen, (C) SNAP25 frozen, and (D) Syx and SNAP25 frozen.

In both cases, the results differ from those seen in Fig. 4 when unraveling was not permitted. For the case of hydration repulsion, the minimum separation is somewhat larger (~ 2.4 nm) than that shown in Fig. 4 B (~ 2.1 nm). There is a similar difference for the case of electrostatic repulsion.

10.5. Freezing SNAP25 or Syx: In our simulations we allowed SNAP25 helices to be free to adjust their orientation. This mimics the optical tweezers experiment used to calibrate our model. However, the situation *in vivo* is likely different with SNAP25 and/or Syx constrained against motion. In order to see the effects of the positioning of SNAP25 in relation to the SNARE bundle we studied three variations: freezing Syx, freezing SNAP25, and freezing both Syx and SNAP25. When Syx was frozen, SNAP25 still remained associated with Syb. Anytime that SNAP25 was frozen at all, it remained associated with Syx. The energy calculations were repeated for the hydration repulsion case (Fig. S11) and the electrostatic repulsion case with fixed surface charge (Fig. S12). The freezing of helices in all of these cases has little effect on the minimum distance and number of SNAREs. The principal difference occurs for the one-SNARE case where the equilibrium distance reduces significantly.

10.6. High Osmotic Pressure and Low Pretension Limit

Figs. 2 and S7 show cases of low osmotic pressure and plasma membrane tension where the plasma membrane bulges near the axis of symmetry because the attractive forces draw the two membranes to each other at their point of application but near the axis of symmetry only repulsion acts. Experiments suggest that prior to vesicle to membrane fusion, the vesicle retains its spherical shape while the plasma membrane surface conforms when the two are in contact (13, 14). The continuum model was recalculated using high osmotic pressure in the vesicle and low pretension in the plasma membrane with constant potential. The resulting structures are shown for 10 and 15 SNAREs in Fig. S16.

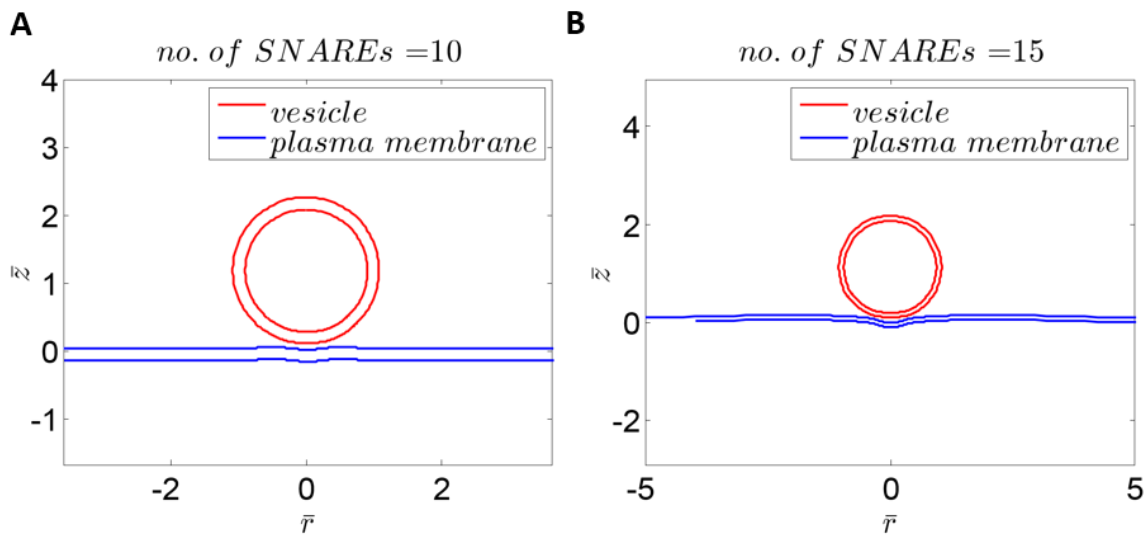


FIGURE S13 For a 20nm vesicle with high osmotic pressure and low pretension in the plasma membrane with constant potential the vesicle and plasma membrane structures are shown including their bilayer thickness for (A) 10 SNAREs and (B) 15 SNAREs.

Under the conditions of high osmotic pressure and low pretension when 10 SNAREs are present there is little bulging of the plasma membrane and the vesicle remains spherical when the vesicle and plasma membrane are brought together. The separation is relatively constant which is consistent with the Malsam et al.(13) and Hernandez et al. (14). As the number of SNAREs is increased to 15, there is some bulging in the plasma membrane at the axis of symmetry. The vesicle has retained its spherical shape while the plasma membrane bends to conform to it.

The energy surface for this case is shown in Fig. S14. We note that there is little difference between these and those of Fig. 4 B. This suggests that our model is robust with respect to this uncertainty. (In particular, the value of vesicle osmotic pressure is difficult to estimate.)

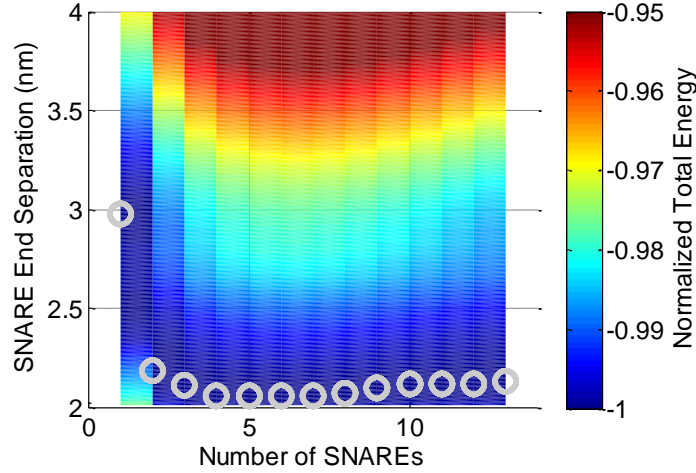


FIGURE S14 Contour of normalized total energy as a function of SNARE end separation and number of SNAREs for a 20nm vesicle with high osmotic pressure and low pretension in the plasma membrane, and with constant potential on the vesicle and plasma membrane. White circles correspond to energy minima representing the equilibrium SNARE end separation for a given number of SNAREs.

10.7. High Vesicle Pressure, High Membrane Tension Vesicle-Membrane Model

In order to display the effects of the deformation considered in the continuum model, a more simplified analytical model of the Vesicle-Membrane system based on Bykhovskaia et al.(15) was calculated. The parameters used in the analytical model were consistent with those used in the continuum model as described in Section 2.3. Consider the case in which vesicle pressure P_o and the membrane tension T are sufficiently large such that neither the vesicle nor the membrane deform as they approach each other. In this case Bykhovskaia et al.(15) have shown that the force between the vesicle and membrane is given by

$$F = \frac{2\pi R \epsilon \epsilon_0}{l_D} \left(\frac{2\varphi_1 \varphi_2}{\sinh\left(\frac{a}{l_D}\right)} - (\varphi_1^2 + \varphi_2^2) \left(\coth\left(\frac{a}{l_D}\right) - 1 \right) \right) \quad (\text{S18})$$

for fixed surface potential and

$$F = \frac{\pi R l_D}{\epsilon \epsilon_0} \left(\frac{2\sigma_1 \sigma_2}{\sinh\left(\frac{a}{l_D}\right)} + (\sigma_1^2 + \sigma_2^2) \left(\coth\left(\frac{a}{l_D}\right) - 1 \right) \right) \quad (\text{S19})$$

for fixed charge. The force separation curves are shown for the vesicle-plasma membrane for several cases using this model in Figs. S15 and S16.

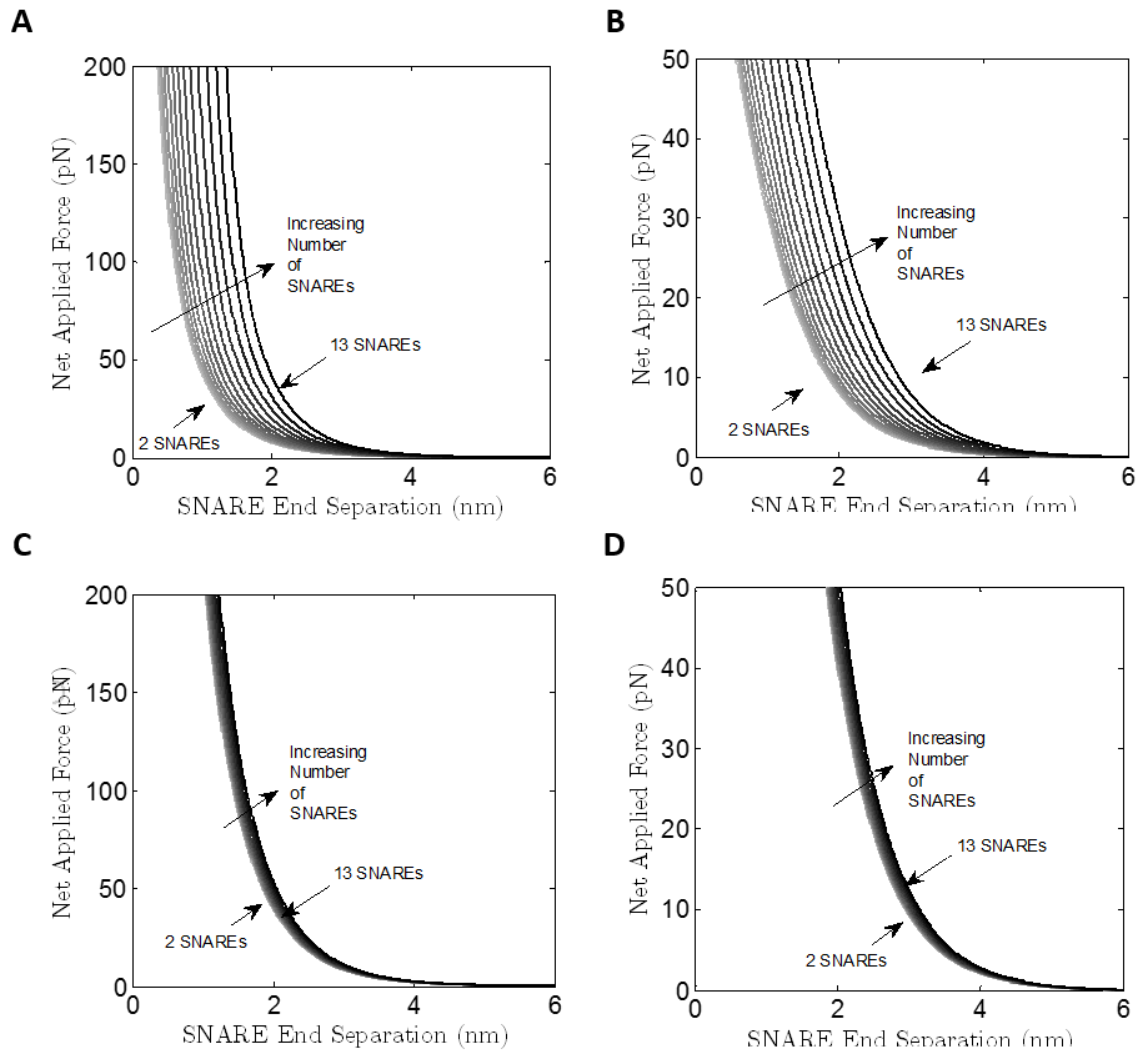


FIGURE S15 For the high vesicle pressure high membrane tension limiting case, the net applied force in the membrane/vesicle system is shown as a function of SNARE end separation for a vesicle with a (A) 20nm radius with fixed charge, (B) 20nm radius with fixed surface potential, (C) 100nm radius with fixed charge, and (D) 100nm radius with fixed surface potential.

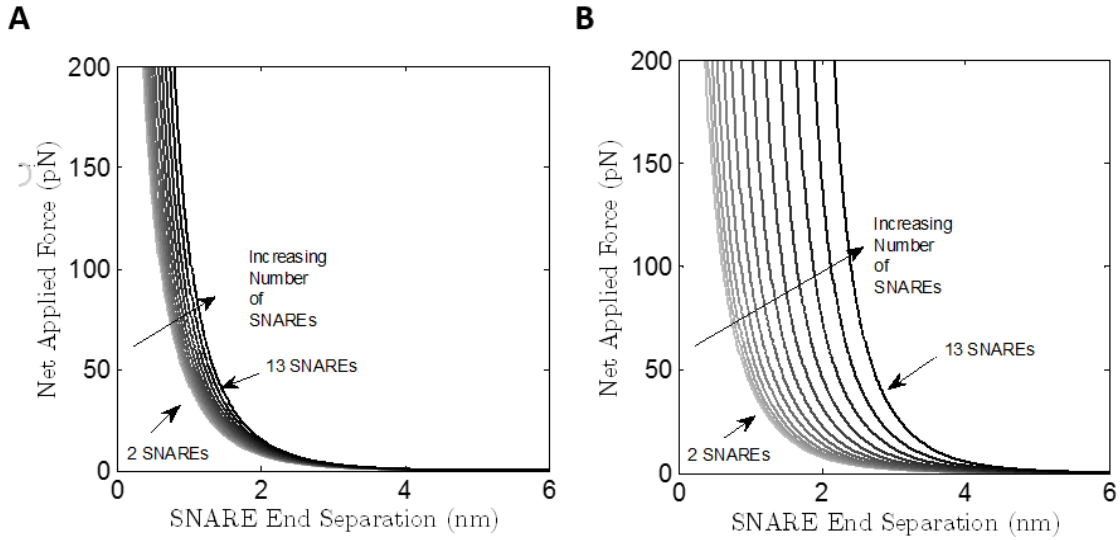


FIGURE S16 For the high vesicle pressure high membrane tension limiting case, the net applied force in the membrane/vesicle system is shown as a function of SNARE end separation for a radius for a vesicle with a 20nm radius with fixed charge when (A) the SNARE bundle diameter is 2nm and (B) the SNARE bundle diameter is 4nm.

10.8. Effect of Lateral Bundle Width: Figure S17 shows results of a test of the sensitivity of the solution to the location of the SNAREs when the lateral size of the SNARE bundle was varied from 2nm in Fig. S17 A to 4nm in Fig. S17 B (the base case used is 3nm, Fig. 4 B). Increasing the lateral width of the SNARE bundle seems to have a significant effect on the solution. There is a minimum separation at 4 SNAREs. With the addition of more than 5 SNAREs the equilibrium separation again begins to increase all the way up to ~3nm with 13 SNAREs.

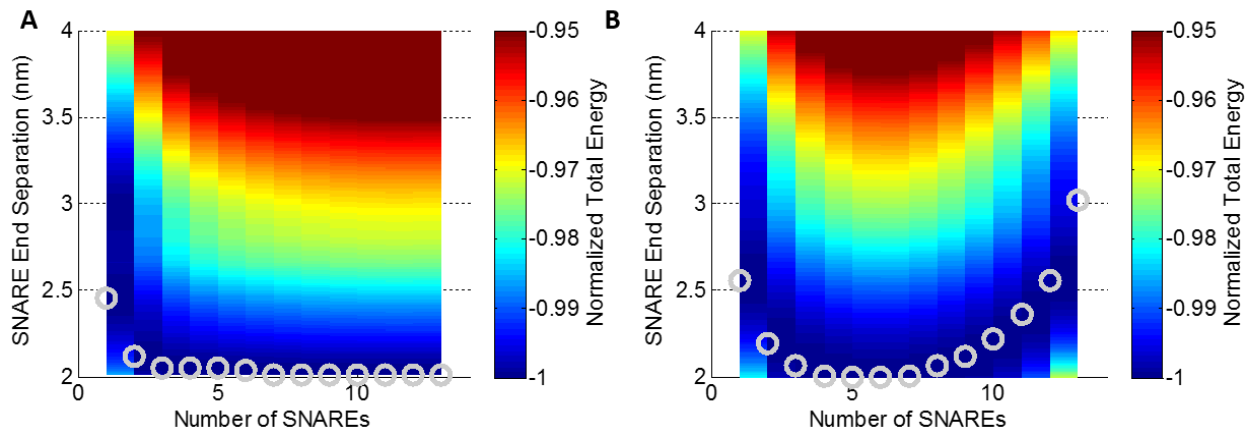


FIGURE S17 For the high pressure high tension limiting case, contour plots of normalized total energy as a function of SNARE end separation distance and the number of SNAREs are shown. Gray circles correspond to energy minima representing the equilibrium SNARE end separation for a given number of SNAREs. Several cases are shown for the vesicle with a radius of 20nm and fixed charge. The size of the SNARE bundle was varied to (A) 2nm and (B) 4nm.

11. SUPPORTING REFERENCES

1. Schlick, T. 2002. *Molecular modeling and simulation: an interdisciplinary guide*. New York: Springer.
2. Kubo, R. 2002. The fluctuation-dissipation theorem. *Reports Prog. Phys.* 29: 255–284.
3. Gao, Y., S. Zorman, G. Gundersen, Z. Xi, L. Ma, G. Sirinakis, J.E. Rothman, and Y. Zhang. 2012. Single reconstituted neuronal SNARE complexes zipper in three distinct stages. *Science*. 337: 1340–3.
4. Bruce Alberts, Julian Lewis, Keith Roberts, and Peter Walter, Alexander Johnson, M.R. 2002. *Molecular Biology of the Cell*. 4th ed. New York: Garland Science.
5. Ohsawa, K., H. Ohshima, and S. Ohki. 1981. Surface potential and surface charge density of the cerebral-cortex synaptic vesicle and stability of vesicle suspension. *Biochim Biophys Acta*. 648: 206–214.
6. Marra, J. 1986. Direct measurement of the interaction between phosphatidylglycerol bilayers in aqueous electrolyte solutions. *Biophys. J.* 50: 815–825.
7. Pekker, M., and M.N. Shneider. 2014. The surface charge of a cell lipid membrane. *arXiv Prepr. arXiv.* : 1401–1407.
8. Deserno, M. *Fluid lipid membranes – a primer*. 2007. http://www.cmu.edu/biolphys/deserno/pdf/membrane_theory.pdf
9. Kweon, D.H., C.S. Kim, and Y.K. Shin. 2002. The membrane-dipped neuronal SNARE complex: A site-directed spin labeling electron paramagnetic resonance study. *Biochemistry*. 41: 9264–9268.
10. Kweon, D.-H., C.S. Kim, and Y.-K. Shin. 2003. Regulation of neuronal SNARE assembly by the membrane. *Nat. Struct. Biol.* 10: 440–447.
11. Kim, C.S., D.H. Kweon, and Y.K. Shin. 2002. Membrane topologies of neuronal SNARE folding intermediates. *Biochemistry*. 41: 10928–10933.
12. Stein, A., G. Weber, M.C. Wahl, and R. Jahn. 2009. Helical extension of the neuronal SNARE complex into the membrane. *Nature*. 460: 525–528.
13. Malsam, J., D. Parisotto, T.A.M. Bharat, A. Scheutzow, J.M. Krause, J.A.G. Briggs, and T.H. Söllner. 2012. Complexin arrests a pool of docked vesicles for fast Ca²⁺-dependent release. *EMBO J.* 31: 3270–3281.

14. Hernandez, J.M., A. Stein, E. Behrmann, D. Riedel, A. Cypionka, Z. Farsi, P.J. Walla, S. Raunser, and R. Jahn. 2012. Membrane Fusion Intermediates via Directional and Full Assembly of the SNARE Complex. *Science* (80-.). 336: 1581–1584.
15. Bykhovskaia, M., A. Jagota, A. Gonzalez, A. Vasin, and J.T. Littleton. 2013. Interaction of the complexin accessory helix with the C-terminus of the SNARE complex: molecular-dynamics model of the fusion clamp. *Biophys J.* 105: 679–690.